RSC Advances

ROYAL SOCIETY OF CHEMISTRY

PAPER

View Article Online
View Journal | View Issue

Cite this: *RSC Adv.*, 2024, **14**, 10113

Synthesis of different organic ammonium-based bismuth iodide perovskites for photodetection application†

Amr Elattar, *[a] Cassie Duclos,[a] Franchesca Bellevu,[a] Tarik Dickens*[a] and Okenwa Okoli [ab]

Received 7th January 2024
Accepted 13th March 2024

DOI: 10.1039/d4ra00173g

rsc.li/rsc-advances

Bismuth-based perovskites are promising candidates for highly stable halide perovskites with low toxicity. Here, we report the synthesis of a series of bismuth iodide-based perovskites with different primary, secondary, and tertiary ammonium cations and study their structural, thermal, and optical properties, and the likelihood of photodetection. Interestingly, the variation of A-site organic ammonium cations, with different interlayer spacings between adjacent bismuth iodide monolayers, has exotic effects on the diffraction patterns and morphological structures of the perovskite crystals. Thermogravimetric analysis reveals the highest thermal stability of tertiary ammonium-based bismuth perovskite with a decomposition temperature of 385 °C. The branched primary ammonium-based photodetector has photo-responsivity roughly two and four times faster than that of secondary and tertiary ammonium-based devices, respectively. These findings provide insight into the importance of A-site cation engineering for structural modulation and tailoring the optoelectronic properties of bismuth-based perovskites for emerging optoelectronic devices.

Introduction

Organic-inorganic hybrid perovskites (OIHPs) have shown a great interest in various optoelectronic applications owing to their unique characteristics such as high absorption coefficient,[1] tunable bandgap,[2–6] high carrier mobility,[7–11] and low-cost preparation.[12–16] Lead halide perovskites research has received a lot of attention in the scientific community recently. However, their toxicity and their environmental threat make lead perovskites an unideal choice for commercial uses.[17–24] Thus, lead-free perovskites are now being investigated.[25–31] One of the lead-free perovskites is bismuth, which may present a suitable replacement for lead where Bi^{3+} is isoelectric with Pb^{2+}, having the same number of valence electrons. Furthermore, organic bismuth halide perovskites have been reported to be highly stable to ambient air and humidity over long periods.[32] In addition, Bi^{3+} works as a photosensitizer that can drive exciton emission of bismuth-containing double perovskites;[33] therefore, it is likely to work similarly in Bi-based perovskites. Finally, bismuth is a nontoxic earth-abundant element, making it more appealing than lead for commercial devices. For example, $MA_3Bi_2I_9$ ($MA = CH_3NH_3^+$) perovskite has shown potential use in solar cells,[34–37] photodetector,[38] light-emitting diodes,[39] and X-ray imaging.[40,41] Furthermore, Hu *et al.* developed a 3D-$MAPbI_3$/2D-$MA_3Bi_2I_9$ perovskite heterostructure with higher efficiency and improved stability compared to lead perovskite.[42] Beyond $MA_3Bi_2I_9$, different organic cations-based bismuth perovskites have been investigated. The team by Fabian *et al.* compared the HDA_2BiI_{10} (HDA = hexane-1,6-diammonium) perovskite with an analogous perovskite containing n-propyl ammonium cations instead of the diammonium cation; they found that the diammonium perovskite had a more symmetric orthorhombic structure compared to the triclinic structure of the ammonium perovskite and was more resistant to thermal treatments than the ammonium perovskite and also predicted that the diammonium perovskite had a small band gap of ~2 eV.[43] Wang *et al.* synthesized a heptane-1,7-diammonium-based bismuth perovskite $[NH_3(CH_2)_7NH_3][BiI_5]$ with a low bandgap at 1.89 eV and structural phase transition point as high as 351.7 K.[44]

Bismuth-based perovskite materials have been devoted to photodetection applications.[45,46] Tong *et al.* developed a highly stable $CsBi_3I_{10}$ perovskite-based red-light photodetector with better responsivity and specific detectivity than lead halide perovskite devices.[47] Moreover, Eckhardt *et al.* constructed an antisolvent-assisted $MA_3Bi_2I_9$ perovskite single crystal-based photodetector with fast response times.[48] Furthermore, Bhorde *et al.* fabricated $MA_3Bi_2I_9$ and MA_2BiI_5 perovskite thin film-based photodetectors, finding that both have a fast response and

[a]*Industrial & Manufacturing Engineering, FAMU-FSU College of Engineering, 2525 Pottsdamer St., Tallahassee, Florida, 32310, USA. E-mail: ae23e@fsu.edu; dickens@eng.famu.fsu.edu*

[b]*Herff College of Engineering, University of Memphis, Memphis, TN, 38111, USA*

† Electronic supplementary information (ESI) available. See DOI: https://doi.org/10.1039/d4ra00173g

recovery time as well as very stable switching behaviour.[38] Moreover, Shah *et al.* revealed that 2-methoxyethanol is the best solvent choice for the best coverage, smallest grain size, good optical properties, and better photo-response of the $MA_3Bi_2I_9$ perovskite thin film-based photodetector.[49] Mixed halides (Cl/I) of $MA_3Bi_2I_6Cl_3$-based photodetector have been reported to obtain photo-responsivities and specific detectivities roughly three times greater than pristine $MA_3Bi_2I_9$-based devices.[50] In addition, one research work has also been reported with diammonium bismuth perovskites. Ji *et al.* fabricated photodetector arrays from (TMHD)$BiBr_5$ (TMHD = *N*,*N*,*N*,*N*-tetramethyl-1,6-hexanediammonium) perovskite single crystals with large on/off current ratios and high response rate.[51] One key for the structural modulation of perovskite materials is organic cation (A-site) engineering.[52] Few works have been devoted to A-site engineering of Bi-based perovskites. For instance, incorporation of PEA as an organic spacer into 3D $Cs_2AgBiBr_6$ leads to enhancing cations ordering and decrease of perovskite dimensionality into 2D $(PEA)_2CsAgBiBr_7$.[53,54] Furthermore, four different Ag–Bi double perovskites $(RA)_4AgBiBr_8$, with different thin film structures have been reported, where RA = hexylammonium (HA), butylammonium (BA), isobutylammonium (IBA), and phenylethylammonium (PEA).[55]

Herein, we have investigated four different primary, secondary, and tertiary amines-based bismuth iodide perovskites. X-ray diffraction (XRD) patterns show that the formed Bi-perovskite samples have different crystal structures. Tertiary amine-based (TEA) perovskite shows the highest thermal stability with a decomposition temperature of 385 °C. Optical measurements indicate a minor impact of change in the organic cation on the bandgap energies of bismuth iodide perovskites. The four different organic cation-based bismuth perovskites have shown a good tendency towards photodetection applications where the branched IBA-based perovskite device has the best photo-responsivity and photo-detectivity compared to other devices.

Experimental

Materials

All chemicals were obtained from Sigma-Aldrich unless otherwise noted. Chemicals used were bismuth(III) iodide, 99%; *N*,*N*′-dibenzylethylenediamine, 99%; triethylamine, 99%; isobutylamine, 99%; butylamine, 99%; and tin oxide, 15% in H_2O colloidal dispersion from Alfa Aesar. Additionally, a solution of hydroiodic acid, 57 wt%, with added hypophosphorous acid for stability was used. *N*,*N*-Dimethylformamide (DMF), 99%; dimethylsulfoxide (DMSO), 99%; dichloromethane (DCM), 99%; and methanol, 99%, were used as solvents. Isopropanol, 99%, was used for cleaning equipment and substrates. Helman III from Hellma Analytics, nano pure water, and acetone were used for cleaning substrates. Glass/ITO substrates were used for the fabrication of photodetector devices.

Synthesis of bismuth-based perovskites

Four different organic amines, *i.e.*, *N*,*N*′-dibenzylethylenediamine (DBED), triethylamine (TEA), isobutylamine (IBA), and butylamine (BA), were used to prepare Bi-perovskite materials. First, ammonium cations were prepared by reacting the monoamines (TEA, IBA, and BA) with equimolar amounts of hydroiodic acid in a solution with hypophosphorous acid *via* drop-wise addition, while the diamine (DBED) was reacted with two molar equivalents of the same. The solutions were heated at 80 °C for 24 h to evaporate the solvent and retrieve the ammonium iodide salts as white crystals. The ammonium iodide salts were washed with dichloromethane (DCM) and dried. Secondly, to prepare perovskite solutions, all ammonium salts were placed in vials with specific molar ratios of bismuth(III) iodide and monoammonium iodide salts, a 3 : 2 ratio of monoammonium iodide salt (TEA, IBA, or BA) to bismuth(III) iodide, and for the diammonium iodide salt (DBED), a 1 : 1 ratio of DBED to bismuth(III) iodide. A solvent of DMF : DMSO at a 4 : 1 (V/V) ratio was added to each vial to make a 0.5 M perovskite solution. Solutions were vortexed for 2 min and then placed on a hotplate with strong stirring at 90 °C for 1–2 h, or until the solution was clear. After that, perovskite solutions were filtered using a PTFE syringe filter to be ready for further steps.

Bismuth perovskite thin films with good coverage were prepared by spin coating of the perovskite solutions over pre-heated substrates at 1000 RPM for 5 s and then 4500 RPM for 30 s and annealed at 120 °C for 10 min, as shown in Fig. 1a. Substrates were pre-heated for 5 min at 120 °C and the solution was placed onto them for 10 s before being moved to the spin coater for spin coating. To obtain bismuth perovskite powders, perovskite solutions were drop-cast onto glass substrates and dried on a hot plate at 120 °C. Powders were obtained after solvent evaporation, as depicted in Fig. 1b.

Fabrication of bismuth perovskite-based photodetectors (PDs)

ITO-coated glass substrates were etched using zinc powder and hydrochloric acid (HCl). Then, ITO substrates were cleaned using the Helman III diluted detergent, deionized water, acetone, and isopropanol, under sonication for 15 min with each solvent. Finally, ITO substrates were treated with ozone plasma for 15 min. For electron transport layer (ETL) assembly, 200 μL of 15% SnO_2 in H_2O was dropped over ITO. They were spun for 5 s at 1000 RPM and then for 30 s at 4500 RPM. After spin coating, they were annealed at 120 °C for 30 min to obtain the SnO_2 layer with 900 nm thickness. ITO/SnO_2 cells were

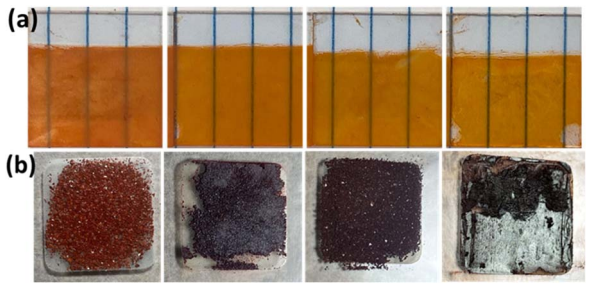

Fig. 1 (a) Spin-coated perovskite thin film slides. (b) Perovskite powders obtained *via* a drop casting method. From left to right: DBED, TEA, IBA, BA bismuth perovskites.

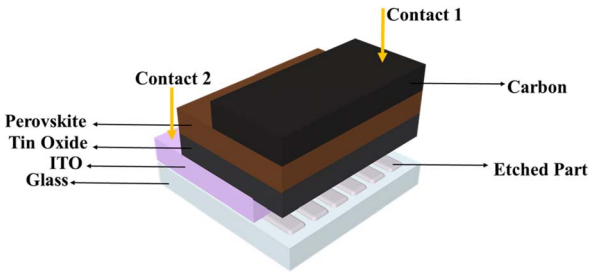

Fig. 2 Perovskite photodetector cell configuration.

further treated with ozone plasma for 15 min. Then, 200 μL of each bismuth perovskite solution was spin-coated over ITO/SnO_2 for 5 s at 1000 RPM and then for 30 s at 4500 RPM before being placed on a hot plate to anneal at 120 °C for 30 min. The obtained perovskite layer has a 4 μm thickness. Finally, carbon metal contact was deposited over the perovskite layer by doctor blading of the carbon paste by annealing at 120 °C for 1 h to obtain the carbon layer with 40 μm thickness. The perovskite cell configuration is shown in Fig. 2.

Characterization

The film morphology was studied by scanning electron microscopy (SEM, Thermo Fisher). The X-ray diffraction (XRD) measurement was performed by employing the Rigaku Smart lab diffractometer. The absorption of the samples was measured using a UV-vis spectrophotometer (Cary UV-2450). Thermogravimetric analysis was performed by TGA (TA Instruments). The current–voltage (*I–V*) and current–time (*I–t*) characteristics of the photodetector were measured using the Keithley 2400 system source meter that was attached to a computer through a GPIB 488A interface. For white light illumination, a Sinus-70 solar simulator (WAVELABS Solar Metrology Systems GmbH) was used for measuring the photoresponse of the fabricated ITO/SnO_2/Bi-perovskite/carbon device. The photocurrent-time characteristic curves were measured under standard AM 1.5 sunlight (100 mW cm^{-2}). Fig. 2 shows a perovskite photodetector cell configuration. All measurements were performed under ambient atmosphere.

Results and discussion

Four different types of organic ammonium salts were utilized to prepare Bi-perovskites, as depicted in Fig. 3; DBED has a diammonium cation with two secondary amines. TEA has a monoammonium cation with a tertiary amine. IBA and BA have monoammonium cations with branched and unbranched primary amines, respectively. The perovskite crystal powders obtained *via* the drop-casting method have shown different morphological structures (Fig. S1†). While TEA perovskite has unorganized coagulated structure (Fig. 5b), DBED and IBA perovskites have layered stacked structures (Fig. 5a and c, respectively). Furthermore, BA perovskite has hexagonal structure (Fig. 5d), which is consistent with hexagonal structure of primary unbranched ammonium (methyl ammonium, MA)-based perovskite $MA_3Bi_2I_9$.[41] The homogeneous distribution of C, N, Bi, and I elements in Bi-perovskite structures was also confirmed *via* the elemental mapping of EDS, as shown in Fig. S2–S5.†

To characterize the different organic cation Bi-based halide perovskites, we obtained the X-ray diffraction (XRD, Bruker) data. Diffraction patterns of Bismuth perovskites are different from patterns of their corresponding ammonium iodide precursors, as illustrated in ESI Fig. S6.† Thus, it can be inferred that the perovskite powders were prepared. XRD plots of DBED, TEA, IBA, and BA perovskites show different diffraction peaks, suggesting their possession of different crystal structures (Fig. 4a). Related to the main diffraction peak, 2θ values were 7.19°, 7.72°, 7.96°, and 7.24° with a *d*-spacing of 12.3, 11.5, 11.1, and 12.2 Å for DBED, TEA, IBA, and BA, respectively (Fig. 4b and S7†). The shifting of *d*-spacing in the order of DBED > BA > TEA > IBA is consistent with their organic cation molecular steric size where the molecule length of DBED, TEA, IBA, and BA amines was estimated to be 15.60 Å, 6.22 Å, 4.61 Å, and 6.46 Å, respectively.

Different morphological structures of perovskite thin films were confirmed microscopically by scanning electron microscopy (SEM), as shown in Fig. 5. DBED perovskite exhibits layered structure with cracked grains (Fig. 5a). TEA perovskite film contains two mixed phases where hexagonal-shaped phase embedded in coherent and adjacent rod-like phase (Fig. 5b). IBA and BA perovskites have entangled rod-like structures (Fig. 5c and d). Compared with DBED, TEA, and BA perovskite films with massive pinholes and cracked grains, the IBA perovskite film exhibited much improved pinholes-free film morphology. These results reveal the high impact of the organic cation precursor type to modulate the morphological structure of the as-prepared Bi-perovskites.

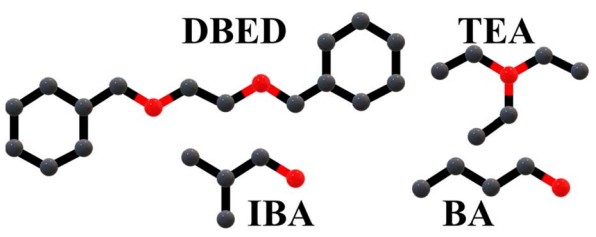

Fig. 3 Four different organic cations utilized as A-site for Bi-perovskites, where C and N atoms are presented as grey and red balls, respectively.

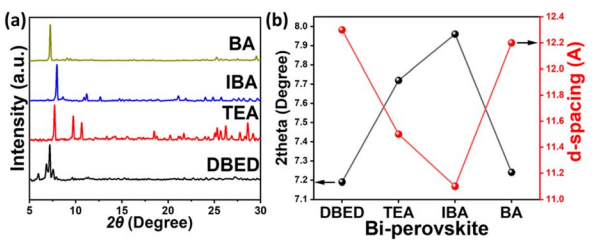

Fig. 4 (a) Powder XRD patterns of different organic cations-based Bi perovskites. (b) Relationship between 2theta/*d*-space values of XRD-main peak (*y*-axis) and Bi-perovskites (*x*-axis).

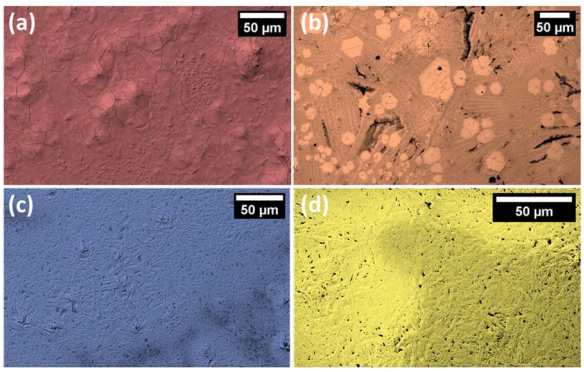

Fig. 5 Scanning Electron Microscope (SEM) images of (a) DBED, (b) TEA, (c) IBA, and (d) BA perovskite films.

Thermal stability was studied for different organic cations of Bi-perovskites through thermogravimetric analysis (TGA) for powder samples obtained by the drop-casting method. The decomposition profiles for DBED, BA, and IBA-based Bi perovskites can be divided into two steps, as shown in Fig. 6. The first step is accompanied by organic ammonium iodide weight loss. The second step is possibly accompanied by the loss of BiI_3. The first weight loss is at 140 °C, 150 °C, and 163 °C for IBA, BA, and DBED perovskites, respectively, which indicates an increase in thermal stability in the order IBA < BA < DBED. This is consistent with boiling point values: 68 °C, 78 °C, and 184 °C for IBA, BA, and DBED amines, respectively. TEA perovskite is the highest thermally stable Bi perovskite with only one decomposition step where its decomposition starts at 385 °C. This can be attributed to the presence of a tertiary-typed triethyl ammonium group through the TEA perovskite structure where the high stability of the nitrogen atom is attributed to three donating (ethyl) groups. As a result, a strong interaction arises between the TEA organic cation and BiI_3 inorganic slag, which requires more thermal energy for decomposition. Overall, based on TGA results, the thermal stability of Bi perovskites depends on the type of the amine group of the organic cation where thermal

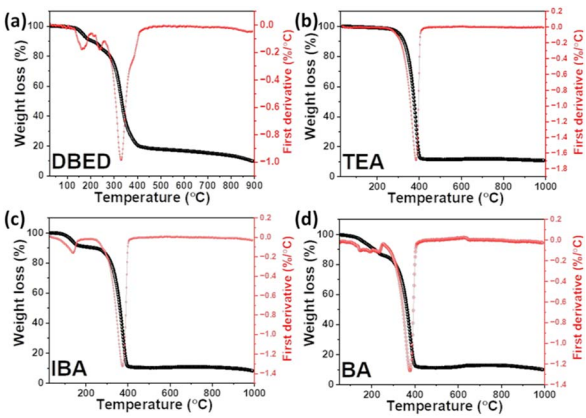

Fig. 6 TGA analysis of (a) DBED, (b) TEA, (c) IBA, and (d) BA perovskite powders.

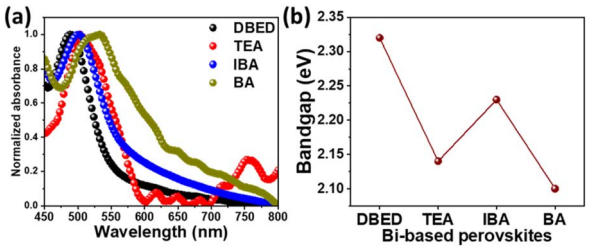

Fig. 7 Normalized absorbance (a), and bandgap values (b) of Bi perovskites.

stability of tertiary amine TEA perovskite > secondary amine DBED perovskite > primary amine IBA/BA perovskites.

UV-vis absorption spectra of different organic cations-based Bi perovskite thin films are shown in Fig. 7. Absorption peaks are shifted towards higher wavelengths in the order of DBED < IBA < TEA < BA. Tauc plots show that the optical bandgap energies of the perovskites are 2.32 eV for DBED, 2.14 eV for TEA, 2.23 eV for IBA, and 2.10 eV for BA-perovskites (Fig. 7b and S8†). The lower bandgaps of TEA and BA perovskite thin films are consistent with their color darkness. Overall, a change of organic cation has a minor effect on the optical properties of bismuth perovskites, compared with a change of halides.[56]

Perovskite-based photodetectors (PPDs) transform incident radiation into electrical signals with a halide perovskite layer within the detector acting as a photon absorber. The photo-current response measurements of the perovskite-based photodetector devices allow them to be compared to one another. Thus, time-resolved photo-current response (on/off) measurements were conducted under alternating dark and light illumination (100 mW cm^{-2}), within time intervals (10 seconds/each) at zero bias voltage. Graphs of time-resolved photo-response [(I–t) curves] of DBED, TEA, IBA, and BA perovskite photodetectors are depicted in Fig. 8a–d, respectively.

Generally, bismuth-based photodetectors show repeatable photo-response. For DBED and IBA PPDs, sharp rise/decay of

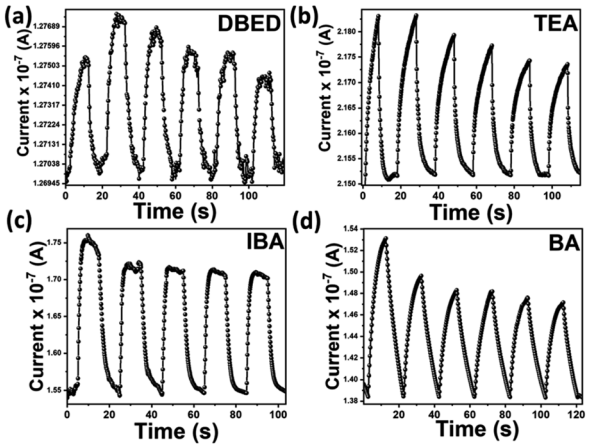

Fig. 8 The transient I–t (ON/OFF) curves of the devices of (a) DBED, (b) TEA, (c) IBA, and (d) BA perovskite-based photodetectors.

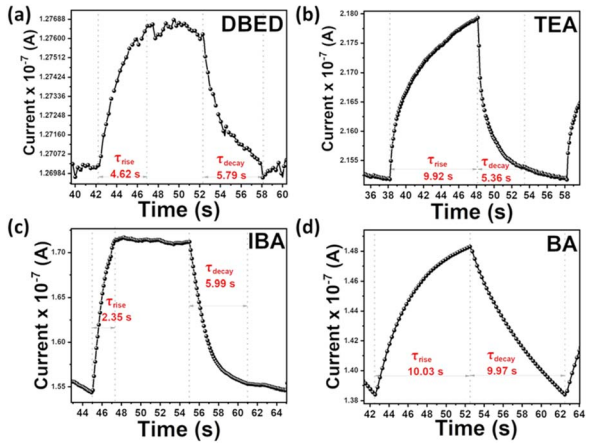

Fig. 9 The single cycle photo-response of (a) DBED, (b) TEA, (c) IBA, and (d) BA perovskite-based photodetectors to estimate the response and recovery time.

photocurrent responses are observed, upon ON/OFF white light illumination, respectively, revealing their fast response/recovery characteristics. This is consistent with previously reported Bi-based perovskite photodetectors. However, TEA PPD shows a gradual rise and fast decay of the photocurrent responses. Moreover, BA PPD reveals a gradual rise/decay of the photocurrent responses signifying its slow response/recovery characteristics. Highlighting on a single ON/OFF cycle of each PPD, the response and recovery time have been evaluated, as depicted in Fig. 9a–d. The response τ_{rise}, and decay τ_{decay} times of the DBED photodetector were found to be 4.62 and 5.79 s, respectively; for the TEA photodetector, they were 9.92 and 5.36 s, respectively; for the IBA photodetector, they were 2.35 and 5.99 s, respectively; and for the BA photodetector, they were 10.00 and 9.97 s, respectively.

Various parameters were calculated to track the performance of the fabricated PPDs, as shown in Table 1, where IBA PPD is considered the best-fabricated bismuth perovskite-based photodetector. The first parameter is the photoresponsivity (R_λ) of a photodetector, which is defined as the photo-current generated through the effective photodetector area per incident light unit power. The photo-responsivity is expressed by eqn (1), where ΔI is the photo-current change under the effect of light illumination $\Delta I = I_{Light} - I_{Dark}$, A is the effective area of the photodetector (4.25 cm^2), and P_λ is the incident light intensity (0.1 W cm^{-2}). The photoresponsivity of DBED, TEA, IBA, and BA PPDs was found to be 1.58, 5.71, 39.35, and 23.45 nA W^{-1}, respectively.

The second parameter is the photosensitivity (ξ) of a photodetector, which is defined as the ratio between the photo-current change under the effect of light illumination and the dark current. The photosensitivity is given by eqn (1). The photosensitivity was estimated to be 0.0054, 0.0126, 0.1113, and 0.0709 for DBED, TEA, IBA, and BA PPDs, respectively. The third parameter is the internal quantum efficiency (IQE) of a photodetector, as given in eqn (3), to estimate the efficiency of the carrier transport, where h is the plank's constant, e is the electron charge, c is the light speed, R_λ is the photoresponsivity, and λ is the wavelength of the incident light. The IQE values of DBED, TEA, IBA, and BA PPDs were found to be 0.391 $\times$ 10^{-6}%, 1.416 $\times$ 10^{-6}%, 9.759 $\times$ 10^{-6}%, and 5.816 $\times$ 10^{-6}%, respectively. The final parameter given by eqn (4), which is related to the photodetector quality, is detectivity (D^*). The detectivity was estimated to be 0.0051 $\times$ 10^4 Jones, 0.0015 $\times$ 10^4 Jones, 11.6945 $\times$ 10^4 Jones, and 7.2040 $\times$ 10^4 Jones, for DBED, TEA, IBA, and BA PPDs, respectively. The higher photo-detectivity of IBA perovskite is consistent with its pinhole-free film morphology. The use of bulk organic cations has shown a negative impact on photo-detectivity. The lower photoresponsivity of DBED and TEA compared with IBA and BA perovskites might be attributed to the higher hydrogen interaction present in higher thermally stable DBED and TEA perovskites, as depicted in TGA analysis. It should be hinted that our bismuth-based photodetectors have shown a lower photodetection performance compared to $MA_3Bi_2I_9$ (MA)-based devices reported in the literature. This might be attributed to the weak interaction between bismuth perovskite and carbon contact through our fabricated devices. As a result, we have prepared MA perovskite, with the same procedure shown in the Experimental section, for comparison with the other prepared perovskites. The MA perovskite thin film exhibited a homogeneous and complete coverage of small hexagonal crystals, as illustrated in Fig. S9.† The MA-based photodetector revealed fast response and recovery characteristics through ON/OFF measurements, as shown in Fig. S10.† The photodetection parameters are presented in Table S1† where the MA-based device exhibited nearly a similar photo-detectivity of BA perovskite. The comparison of different organic cations-based bismuth perovskite photodetectors is shown in Table S2.†

$$R_\lambda = \frac{\Delta I}{P_\lambda \times A} \quad (1)$$

$$\xi = \frac{I_{Photo} - I_{Dark}}{I_{Dark}} \quad (2)$$

Table 1 Photodetector properties of DBED, TEA, IBA, and BA perovskite-based devices

Perovskite PDs	Response time τ_{rise} (s)	Decay time τ_{decay} (s)	Photoresponsivity R_λ (nA W^{-1})	Photosensitivity ξ	Quantum efficiency IQE $\times$ 10^{-6} (%)	Detectivity D^* $\times$ 10^4 (Jones)
DBED	4.62	5.79	1.58	0.0054	0.391	0.0051
TEA	9.92	5.36	5.71	0.0126	1.416	0.0015
IBA	2.35	5.99	39.35	0.1113	9.759	11.6945
BA	10.03	9.97	23.45	0.0709	5.816	7.2040

$$\mathrm{IQE}(\%) = \frac{h \times c \times R_\lambda}{e \times \lambda} \times 100\% \quad (3)$$

$$D^* = \frac{R_\lambda}{(2 \times e \times J_{\mathrm{Dark}})^{\frac{1}{2}}} \quad (4)$$

Conclusions

In summary, bismuth iodide-perovskite crystals with different primary, secondary, and tertiary organic ammonium cations were synthesized by drop-casting of saturated perovskite solutions over glass substrates. We studied their structural, optical, and thermal properties, as well as their photodetection behaviour. XRD and SEM measurements revealed a difference in the diffraction pattern and structural morphology, respectively, of bismuth perovskites depending on the organic cation used. All the spin-coated perovskite thin films show a red color with a bandgap range (2.1–2.3 eV). TGA thermal analysis showed that the triethylammonium tertiary cation (TEA^+) has a higher capability of BiI_3-perovskite structure preservation than other organic ammonium cations with a decomposition temperature of 385 °C. All perovskite-based photodetectors exhibited repeatable ON/OFF photo-response. Butyl (BA) and isobutyl (IBA) primary ammonium cation-based perovskite devices have higher photosensitivity, responsivity, detectivity, and quantum efficiency compared to the secondary and tertiary-based ones.

Author contributions

Amr Elattar conceived the idea for the manuscript and designed the experiments. Amr Elattar and Cassie Duclos synthesized the materials and conducted characterizations. Amr Elattar and Cassie Duclos wrote the first manuscript. All authors discussed the results and commented on the manuscript at all stages. Okenwa Okoli and Tarik Dickens led the project and provided editing.

Conflicts of interest

There are no conflicts to declare.

Acknowledgements

Authors acknowledge the NNSA MSIPP I-AM EMPOWER'D (Grant No. DE-NA0004004), NSF REU No. 1005016 and 1950500 at the FAMU-FSU College of Engineering, Dr Siegrist lab for XRD usage, and the DOW SURE program for donation of the desktop SEM program.

Notes and references

1 A. W. Faridi, M. Imran, G. H. Tariq, S. Ullah, S. F. Noor, S. Ansar and F. Sher, *Ind. Eng. Chem. Res.*, 2023, **62**, 4494–4502.
2 S. A. Kulkarni, T. Baikie, P. P. Boix, N. Yantara, N. Mathews and S. Mhaisalkar, *J. Mater. Chem. A*, 2014, **2**, 9221–9225.
3 M. R. Filip, G. E. Eperon, H. J. Snaith and F. Giustino, *Nat. Commun.*, 2014, **5**, 5757.
4 E. L. Unger, L. Kegelmann, K. Suchan, D. Sörell, L. Korte and S. Albrecht, *J. Mater. Chem. A*, 2017, **5**, 11401–11409.
5 R. J. Sutton, G. E. Eperon, L. Miranda, E. S. Parrott, B. A. Kamino, J. B. Patel, M. T. Hörantner, M. B. Johnston, A. A. Haghighirad, D. T. Moore and H. J. Snaith, *Adv. Energy Mater.*, 2016, **6**, 1502458.
6 D. Ju, Y. Dang, Z. Zhu, H. Liu, C.-C. Chueh, X. Li, L. Wang, X. Hu, A. K.-Y. Jen and X. Tao, *Chem. Mater.*, 2018, **30**, 1556–1565.
7 L. M. Herz, *ACS Energy Lett.*, 2017, **2**, 1539–1548.
8 C. Motta, F. El-Mellouhi and S. Sanvito, *Sci. Rep.*, 2015, **5**, 12746.
9 Y.-F. Chen and E. Orgiu, *ChemNanoMat*, 2019, **5**, 290–299.
10 J. Lim, M. Kober-Czerny, Y.-H. Lin, J. M. Ball, N. Sakai, E. A. Duijnstee, M. J. Hong, J. G. Labram, B. Wenger and H. J. Snaith, *Nat. Commun.*, 2022, **13**, 4201.
11 T. Liu, W. Tang, S. Luong and O. Fenwick, *Nanoscale*, 2020, **12**, 9688–9695.
12 L. Zheng, A. Nozariasbmarz, Y. Hou, J. Yoon, W. Li, Y. Zhang, H. Wu, D. Yang, T. Ye, M. Sanghadasa, K. Wang, B. Poudel, S. Priya and K. Wang, *Nat. Commun.*, 2022, **13**, 7399.
13 H. Chen, Z. Wei, X. Zheng and S. Yang, *Nano Energy*, 2015, **15**, 216–226.
14 N. Leupold and F. Panzer, *Adv. Funct. Mater.*, 2021, **31**, 2007350.
15 H. Benali, B. Hartiti, Y. Nouri, F. Lmai, A. Batan and P. Thevenin, *Mater. Today: Proc.*, 2020, **30**, 981–983.
16 L. Protesescu, S. Yakunin, O. Nazarenko, D. N. Dirin and M. V Kovalenko, *ACS Appl. Nano Mater.*, 2018, **1**, 1300–1308.
17 E. M. Hutter, R. Sangster, C. Testerink, B. Ehrler and C. M. M. Gommers, *iScience*, 2022, **25**, 103583.
18 C.-H. Chen, S.-N. Cheng, L. Cheng, Z.-K. Wang and L.-S. Liao, *Adv. Energy Mater.*, 2023, **13**, 2204144.
19 M. Ren, X. Qian, Y. Chen, T. Wang and Y. Zhao, *J. Hazard. Mater.*, 2022, **426**, 127848.
20 P. Billen, E. Leccisi, S. Dastidar, S. Li, L. Lobaton, S. Spatari, A. T. Fafarman, V. M. Fthenakis and J. B. Baxter, *Energy*, 2019, **166**, 1089–1096.
21 P. Su, Y. Liu, J. Zhang, C. Chen, B. Yang, C. Zhang and X. Zhao, *J. Phys. Chem. Lett.*, 2020, **11**, 2812–2817.
22 M. Yang, T. Tian, Y. Fang, W.-G. Li, G. Liu, W. Feng, M. Xu and W.-Q. Wu, *Nat. Sustain.*, 2023, **6**, 1455–1464.
23 J. Li, H.-L. Cao, W.-B. Jiao, Q. Wang, M. Wei, I. Cantone, J. Lü and A. Abate, *Nat. Commun.*, 2020, **11**, 310.
24 C. Ponti, G. Nasti, D. Di Girolamo, I. Cantone, F. A. Alharthi and A. Abate, *Trends Ecol. Evol.*, 2022, **37**, 281–283.
25 X. Li, X. Gao, X. Zhang, X. Shen, M. Lu, J. Wu, Z. Shi, V. L. Colvin, J. Hu, X. Bai, W. W. Yu and Y. Zhang, *Adv. Sci.*, 2021, **8**, 2003334.
26 S. Ghosh, H. Shankar and P. Kar, *Mater. Adv.*, 2022, **3**, 3742–3765.
27 Y. Gao, Y. Pan, F. Zhou, G. Niu and C. Yan, *J. Mater. Chem. A*, 2021, **9**, 11931–11943.
28 J. Li, J. Duan, X. Yang, Y. Duan, P. Yang and Q. Tang, *Nano Energy*, 2021, **80**, 105526.

29 E. Aktas, N. Rajamanickam, J. Pascual, S. Hu, M. H. Aldamasy, D. Di Girolamo, W. Li, G. Nasti, E. Martínez-Ferrero, A. Wakamiya, E. Palomares and A. Abate, *Commun. Mater.*, 2022, **3**, 104.
30 W. Ke and M. G. Kanatzidis, *Nat. Commun.*, 2019, **10**, 965.
31 A. E. Magdalin, P. D. Nixon, E. Jayaseelan, M. Sivakumar, S. K. N. Devi, M. S. P. Subathra, N. M. Kumar and N. Ananthi, *Results Eng.*, 2023, **20**, 101438.
32 A. Khan, H. Wen, S. Iqbal, M. Rehman, M. Shah, M. Raheel, F. A. Khan, R. Khan, R. A. Althobiti, E. Alzahrani, A.-E. Farouk, F. F. Al-Fawzan and E. B. Elkaeed, *Opt. Mater.*, 2023, **143**, 114228.
33 B. Wu, W. Ning, Q. Xu, M. Manjappa, M. Feng, S. Ye, J. Fu, S. Lie, T. Yin, F. Wang, T. W. Goh, P. C. Harikesh, Y. K. E. Tay, Z. X. Shen, F. Huang, R. Singh, G. Zhou, F. Gao and T. C. Sum, *Sci. Adv.*, 2023, **7**, eabd3160.
34 M. Lyu, J.-H. Yun, M. Cai, Y. Jiao, P. V Bernhardt, M. Zhang, Q. Wang, A. Du, H. Wang, G. Liu and L. Wang, *Nano Res.*, 2016, **9**, 692–702.
35 B.-W. Park, B. Philippe, X. Zhang, H. Rensmo, G. Boschloo and E. M. J. Johansson, *Adv. Mater.*, 2015, **27**, 6806–6813.
36 C. Momblona, H. Kanda, A. A. Sutanto, M. Mensi, C. Roldán-Carmona and M. K. Nazeeruddin, *Sci. Rep.*, 2020, **10**, 10640.
37 S. Sanders, D. Stümmler, P. Pfeiffer, N. Ackermann, G. Simkus, M. Heuken, P. K. Baumann, A. Vescan and H. Kalisch, *Sci. Rep.*, 2019, **9**, 9774.
38 A. Bhorde, S. Nair, H. Borate, S. Pandharkar, R. Aher, A. Punde, A. Waghmare, P. Shinde, P. Vairale, R. Waykar, V. Doiphode, V. Jadkar, Y. Hase, S. Rondiya, N. Patil, M. Prasad and S. Jadkar, *New J. Chem.*, 2020, **44**, 11282–11290.
39 M. Leng, Z. Chen, Y. Yang, Z. Li, K. Zeng, K. Li, G. Niu, Y. He, Q. Zhou and J. Tang, *Angew. Chem., Int. Ed.*, 2016, **55**, 15012–15016.
40 X. Zheng, W. Zhao, P. Wang, H. Tan, M. I. Saidaminov, S. Tie, L. Chen, Y. Peng, J. Long and W.-H. Zhang, *J. Energy Chem.*, 2020, **49**, 299–306.
41 Y. Liu, Z. Xu, Z. Yang, Y. Zhang, J. Cui, Y. He, H. Ye, K. Zhao, H. Sun, R. Lu, M. Liu, M. G. Kanatzidis and S. Liu, *Matter*, 2020, **3**, 180–196.
42 Y. Hu, T. Qiu, F. Bai, W. Ruan and S. Zhang, *Adv. Energy Mater.*, 2018, **8**, 1703620.
43 D. M. Fabian, A. M. Ganose, J. W. Ziller, D. O. Scanlon, M. C. Beard and S. Ardo, *ACS Appl. Energy Mater.*, 2019, **2**, 1579–1587.
44 Z. Wang, P. Wang, X. You and Z. Wei, *Eur. J. Inorg. Chem.*, 2022, **2022**, e202200172.
45 A. A. Hussain, *ACS Appl. Mater. Interfaces*, 2020, **12**, 46317–46329.
46 A. A. Hussain, A. K. Rana and M. Ranjan, *Nanoscale*, 2019, **11**, 1217–1227.
47 X.-W. Tong, W.-Y. Kong, Y.-Y. Wang, J.-M. Zhu, L.-B. Luo and Z.-H. Wang, *ACS Appl. Mater. Interfaces*, 2017, **9**, 18977–18985.
48 K. Eckhardt, N. Pérez, B. Rasche, A. Zeugner, J. Grothe, T. Doert, K. Nielsch and S. Kaskel, *Sens. Actuators, A*, 2019, **291**, 75–79.
49 S. Shah, A. Bhorde, Y. Hase, R. Aher, V. Doiphode, A. Waghmare, A. Punde, P. Shinde, S. Rahane, B. R. Bade, H. M. Pathan, M. Prasad, M. Aleksandrova, S. P. Patole and S. R. Jadkar, *ACS Appl. Electron. Mater.*, 2022, **4**, 2793–2804.
50 V.-H. Vuong, S. V. N. Pammi, S. Ippili, V. Jella, T. Nguyen Thi, K. Sairam Pasupuleti, M.-D. Kim, M. Ji Jeong, J.-R. Jeong, H. Sik Chang and S.-G. Yoon, *Chem. Eng. J.*, 2023, **458**, 141473.
51 C. Ji, P. Wang, Z. Wu, Z. Sun, L. Li, J. Zhang, W. Hu, M. Hong and J. Luo, *Adv. Funct. Mater.*, 2018, **28**, 1705467.
52 L. Peedikakkandy, S. Chatterjee and A. J. Pal, *J. Phys. Chem. C*, 2020, **124**, 10878–10886.
53 M. Pantaler, V. Diez-Cabanes, V. I. E. Queloz, A. Sutanto, P. A. Schouwink, M. Pastore, I. García-Benito, M. K. Nazeeruddin, D. Beljonne, D. C. Lupascu, C. Quarti and G. Grancini, *JACS Au*, 2022, **2**, 136–149.
54 A. Maiti and A. J. Pal, *J. Phys. Chem. C*, 2021, **125**, 16324–16333.
55 F. Schmitz, J. Horn, N. Dengo, A. E. Sedykh, J. Becker, E. Maiworm, P. Bélteky, Á. Kukovecz, S. Gross, F. Lamberti, K. Müller-Buschbaum, D. Schlettwein, D. Meggiolaro, M. Righetto and T. Gatti, *Chem. Mater.*, 2021, **33**, 4688–4700.
56 J. Zhou, P. Xie, C. Wang, T. Bian, J. Chen, Y. Liu, Z. Guo, C. Chen, X. Pan, M. Luo, J. Yin and L. Mao, *Angew. Chem., Int. Ed.*, 2023, **62**, e202307646.